

Characterizations and Modeling of Grown MQS Nanowires with GaInN/GaN Superlattice Structures

Jinjian Yan,^{II} Soma Inaba,^{II} Weifang Lu,^{*} Yang Bao, Yang Sun, Jinchai Li, Motoaki Iwaya, Kai Huang,^{*} Junyong Kang, Tetsuya Takeuchi, Rong Zhang, and Satoshi Kamiyama



Cite This: *Cryst. Growth Des.* 2025, 25, 639–649

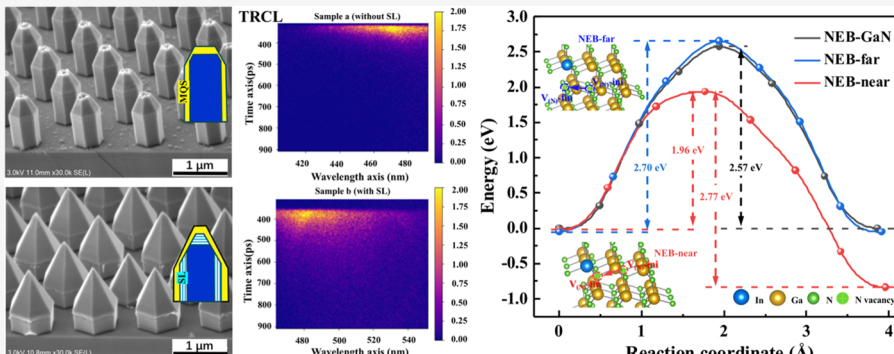


Read Online

ACCESS |

Metrics & More

Article Recommendations



ABSTRACT: The development of the micro-light-emitting diode (Micro-LED) based on GaN nanostructures has brought great prospects for high-quality display applications. In this study, selective-area growth by metal–organic chemical vapor deposition (MOCVD) technology was applied to prepare coaxial GaInN/GaN multi-quantum-shell (MQS) nanowires (NWs) with different crystalline planes. The morphology and emission characterization results demonstrated that the GaInN/GaN superlattices (SLs) effectively reduced the density of point defects in the subsequent grown MQS structures. The NWs containing SLs exhibited larger dimensions and superior emission uniformity on the (10̄11) and (0001)-planes apex region. Moreover, the cathodoluminescence (CL) intensity of NWs with SLs was significantly enhanced, and the time-resolved CL measurements also demonstrated an improvement in crystalline quality. This was mainly attributed to the suppressed migration of point defects to MQS by inserting SLs, thereby improving the crystalline quality of MQSs. We elucidated the mechanism that inhibits the migration of point defects in epitaxial SLs on different crystalline planes through first-principles calculations. Specifically, the calculation indicated that the nitrogen vacancies were preferably localized near In atoms, leading to the suppressed migration of point defects in SLs toward the subsequent growth layer. The variations in growth rates observed among distinct crystalline planes in NWs can be explained by the total energy calculations of atomic adsorption on different crystalline planes and the mechanism of hydrogen passivation. Through the elucidation of the growth mechanism, our study provides valuable insights for optimizing epitaxial growth processes in the development of advanced optoelectronic devices.

1. INTRODUCTION

In recent years, the development of mobile electronic devices and the increasing demand for high-quality display applications have garnered significant attention and research efforts toward GaN-based micro-light-emitting diode (Micro-LED).^{1–3} Compared to traditional display technologies such as liquid crystal display and organic light-emitting diode, Micro-LED offers advantages including high brightness, ultrahigh resolution, short response times, long lifespan, and expansive viewing angles. These remarkable characteristics position Micro-LEDs as highly promising in the field of optoelectronic devices and displays.^{4,5} Nevertheless, it is crucial to solve the challenges associated with scalability and manufacturing processes in achieving uniform brightness and color consistency. Specifi-

cally, AlGaInP-based red Micro-LEDs face severe dimensional effects⁶ and poor temperature stability,⁷ which hinder their application in the red emission segment of full-color Micro-LED displays. In contrast, GaInN materials offer a promising solution to achieve an adjustable band gap in the active region by adjusting the InN fraction, resulting in full coverage of both

Received: October 10, 2024

Revised: January 9, 2025

Accepted: January 10, 2025

Published: January 21, 2025



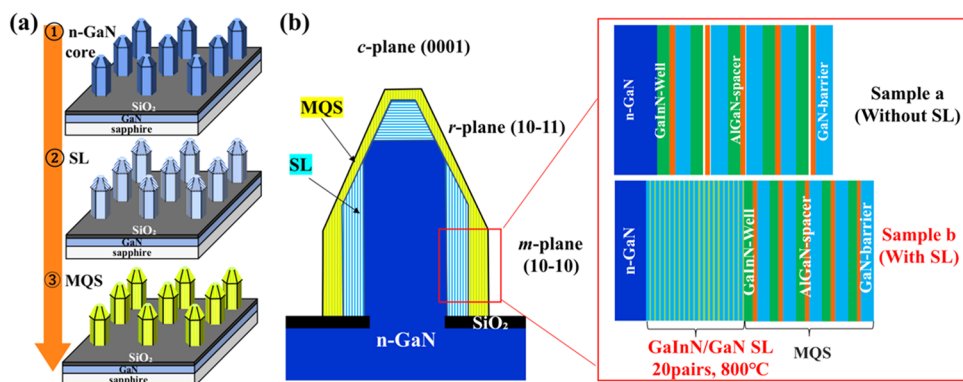


Figure 1. (a) Schematic diagrams of the MQS NW growth with ① n-GaN core, ② GaInN/GaN SL, and ③ five pairs of GaInN/AlGaN spacer/GaN MQS structures. (b) Cross-sectional NWs and detailed MQS structures of the (10 $\bar{1}$ 0)-plane illustrated from n-core side to MQS.

visible spectrum and full-spectrum white LEDs.^{8,9} Consequently, GaInN-based red Micro-LEDs are highly anticipated owing to their compatibility with other GaN-based blue and green LEDs. Moreover, their smaller peak current density makes them more suitable for small-size display devices.^{10,11} However, the heightened In component in GaInN-based red LEDs induces considerable polarization fields and strain within the active layer. These can lead to In composition segregation and trigger a pronounced quantum-confined stark effect (QCSE),¹² ultimately limiting the efficiency of red Micro-LED devices. Additionally, in top-down LED fabrication processes, the employment of dry etching gives rise to plasma-induced damage along the sidewalls of the device. As the dimensions of the device decrease and the perimeter-to-area ratio increases, the size effect of the Micro-LED becomes particularly prominent. This heightened sensitivity to size variations is compounded by surface recombination and the detrimental impact of sidewall damage, both of which bring a substantial increase in strong Shockley–Read–Hall (SRH) recombination.¹³ This leads to a degradation in device efficiency, an increase in leakage current, and a substantial compromise in the overall device performance. To mitigate the sidewall plasma damage caused by dry etching, researchers have employed thermal annealing for lattice restoration¹⁴ and found wet etching to be effective in preventing efficiency degradation caused by sidewall etching damage.^{15,16} Moreover, the application of dielectric sidewall passivation layers such as Al₂O₃¹⁷ and AlN¹⁸ deposited through atomic layer deposition or SiO₂ prepared by plasma-enhanced chemical vapor deposition¹⁹ can eliminate sidewall leakage channels and nonradiative recombination centers, thereby mitigating plasma damage in Micro-LED.

While top-down red GaInN-based Micro-LED technology has indeed made considerable advancements, its light efficiency remains insufficient for practical commercial applications. In contrast, the emerging nanocore–shell structure LEDs exhibit distinctive properties, offering substantial promise.^{20,21} For example, strain relaxation is used to increase InN mole fractions for long-wavelength emission;²² nanoscale size and good heat dissipation are conducive to the development of high-resolution display devices;²³ nanocore–shell structure semipolar and nonpolar surfaces are beneficial for reducing QCSE, stabilizing the emission wavelength at different current densities;^{24,25} most importantly, nanostructure LEDs are made through bottom-up growth processes that eliminate the need for dry etching of active region during device preparation,

avoiding etching damage. To improve device performance, further controlling point defect density is the foundation for achieving high-quality nanowire (NW)-based Micro-LEDs. Based on research findings, introducing AlGaN interlayer and low-In-component GaInN superlattices (SLs) prior to multiple quantum shells (MQSs) has been shown to improve the optical-electric performance of nanostructured devices.^{26,27} However, the physical mechanisms governing the control of the point defect density in SLs remain unclear. Additionally, there are reports indicating that SLs exhibited distinct anisotropy in epitaxial growth characteristics across crystalline planes.²⁶ The growth rate on different crystalline surfaces varies, and there is a lack of explanation for the physical mechanism of alloy component fluctuations combined with epitaxial growth. Therefore, further research is required to understand growth control on each crystalline surface and to investigate defect control for NWs-based devices.

In this work, we elucidate the mechanism of inhibiting point defect migration through epitaxial low-In-component SLs and first-principles calculations. The feasibility of SLs in hindering vacancy defect migration was verified. The formation energy of atomic adsorption on various crystalline planes of NWs was calculated to assess the adsorption stability of different elements. A mechanistic explanation was provided for the anisotropic crystalline surface morphology characteristics observed during the epitaxial growth. Considering the frequent occurrence of hydrogen passivation during epitaxial growth, the growth characteristics of different crystalline planes were simulated. The comparison of the morphology and emission properties between NW samples with and without SLs demonstrated consistency between experiments and theoretical calculation results.

2. EXPERIMENTAL AND CALCULATION DETAILS

NW samples were prepared by selective-area growth in a metal–organic chemical vapor deposition (MOCVD) system (SR 2000, Taiyo Nippon Sanso, Japan). Prior to growth, a SiO₂ mask layer was deposited on the n-GaN/sapphire substrate. The nanoimprint lithography technique was performed to form the pattern of a triangular lattice array with diameters and pitches of 320 and 1200 nm, respectively. The GaN inside the holes was exposed by inductively coupled plasma (ICP) etching (ICPMV06–7001–0, ULVAC, Inc., Chigasaki City, Kanagawa, Japan) system using O₂ and CF₄, which selectively removed the SiO₂ mask. The n-GaN nanocores of all samples were grown at 1150 °C for 95 s to achieve same height as the NWs. To investigate the effect of SLs on the morphology and emission properties of the NWs, samples a and b were grown without and with 20 pairs of GaInN/GaN SLs, as

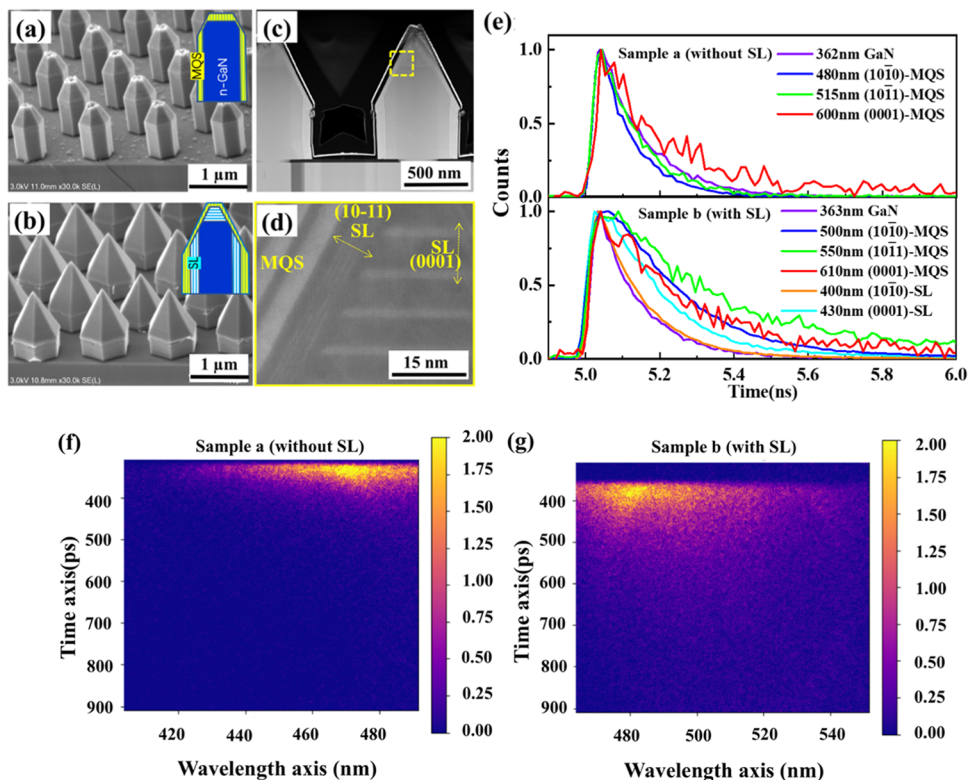


Figure 2. SEM images of NW arrays without SLs (a) and with SLs (b). The insets show the schematic diagrams of the cross-sectional NW. (c) STEM images of the NW structure in sample b. (d) High-magnification STEM image of the junction regions near (0001) and (10 $\bar{1}$)-plane. (e) Normalized TRCL decay curves of (10 $\bar{1}$)-plane region for samples a and b, captured at different wavelengths. Normalized TRCL mappings of the (10 $\bar{1}$)-plane region of (f) sample a and (g) sample b.

illustrated in Figure 1. The SL structure of sample b was grown under a temperature of 800 °C and a pressure of 90 kPa, with growth durations of 1.3 min for the GaN barriers and 0.5 min for the GaInN wells. Following this, both sets of samples underwent epitaxial growth of 5 pairs of MQSs. The GaN barriers were grown at 810 °C for 8.0 min, followed by the growth of AlGaN spacers at 750 °C for 50 s and GaInN wells at 750 °C for 4.3 min. The V/III ratios for the GaInN well/GaN barrier and AlGaN spacer growth were 48,080 and 5770, respectively, under a pressure of 90 kPa.²⁶ The GaN barrier and GaInN well of the SL structures were grown at a temperature of 800 °C and a pressure of 90 kPa for 1.3 and 0.5 min, respectively. The other growth conditions for the n-GaN nanocore and five pairs of GaInN/GaN MQS with AlGaN spacers were identical in samples a and b. For the MQS growth, the GaN barrier, the AlGaN spacer, and the GaInN well were grown at 810 °C for 8.0 min, 750 °C for 50 s, and 750 °C for 4.3 min, respectively.²⁸ For elaborating morphologies characterization and crystalline quality of the MQSs and SLs, the samples were inspected by a scanning electron microscope (SEM-SU5000, Hitachi High-Technologies Co., Tokyo, Japan) and a scanning transmission electron microscope (STEM) (HD2700, Hitachi High-Technologies, Tokyo, Japan). The optical properties of the MQSs were evaluated by using cathodoluminescence (CL) mapping and time-resolved cathodoluminescence (TRCL) measurements (Attolight, Switzerland).

To investigate the epitaxial characteristics of S on NWs, the Vienna Ab initio Simulation Package (VASP) software was utilized to conduct first-principles calculations based on density functional theory (DFT).^{29,30} The projector-augmented wave (PAW) method was used to describe the interactions between the ions and valence electrons. The exchange and correlation function employed in this study was the Perdew–Burke–Ernzerhof (PBE) formulation, which is a specific implementation of the generalized gradient approximation (GGA).³¹ Valence electrons, including Ga_3d and In_3d electrons, were considered, and all calculations were conducted with a plane-

wave cutoff energy of 500 eV. Different slab models were constructed to simulate the adsorption properties of adsorbate atoms on different crystalline surfaces of NWs. Specifically, supercells with dimensions of $4 \times 4 \times 3$, $4 \times 4 \times 4$, and $4 \times 3 \times 4$ were constructed for the (0001), (10 $\bar{1}$ 1), and (1010)-plane structures, respectively. Surface structures with group-III or N atoms were selected for the (0001) and (10 $\bar{1}$ 1)-plane slabs based on the natural growth tendencies of III-nitride materials. The Monkhorst–Pack grids of $4 \times 4 \times 1$ and $4 \times 4 \times 4$ K-points (corresponding to a k-point spacing of $2\pi \times 0.025 \text{ \AA}^{-1}$) were applied for sampling the Brillouin zone of the slab model and bulk material supercell model,^{32,33} respectively. To eliminate the interaction between adjacent supercells caused by periodicity, an 18-Å-thick vacuum layer was introduced in the vertical direction of the slab model and the dangling bonds on the back side of the slab were passivated by fractionally charged hydrogen atoms. During the geometric optimization of the slab model, two molecular layers on the back were fixed, while all of the other atoms were allowed to relax until the total energy of the system reached its minimum value. For all calculations, the geometries of ions were optimized using the conjugate gradient algorithm with energy convergence set at 1×10^{-5} eV.

In order to evaluate the formation characteristics of point defects in NW epitaxial process, the vacancy formation energies on NW surfaces were calculated using formula 1 through first-principles calculation.³⁴

$$E_{f\text{-vacancy}} = E_{\text{vacancy}} - E_{\text{perfect}} + (\Delta n_{V(\text{Ga})} \times \mu_{\text{Ga}} + \Delta n_{V(\text{N})} \times \mu_{\text{N}}) \quad (1)$$

where E_{vacancy} and E_{perfect} represent the total energy of the surface model with and without defects, respectively. The terms $\Delta n_{V(\text{Ga})}$ and $\Delta n_{V(\text{N})}$ refer to the number of Ga vacancies ($V_{(\text{Ga})}$) and N vacancies ($V_{(\text{N})}$) in the model, respectively.

Moreover, the adsorption formation energies E_f of GaN surface atoms were calculated by formula 2.³⁵

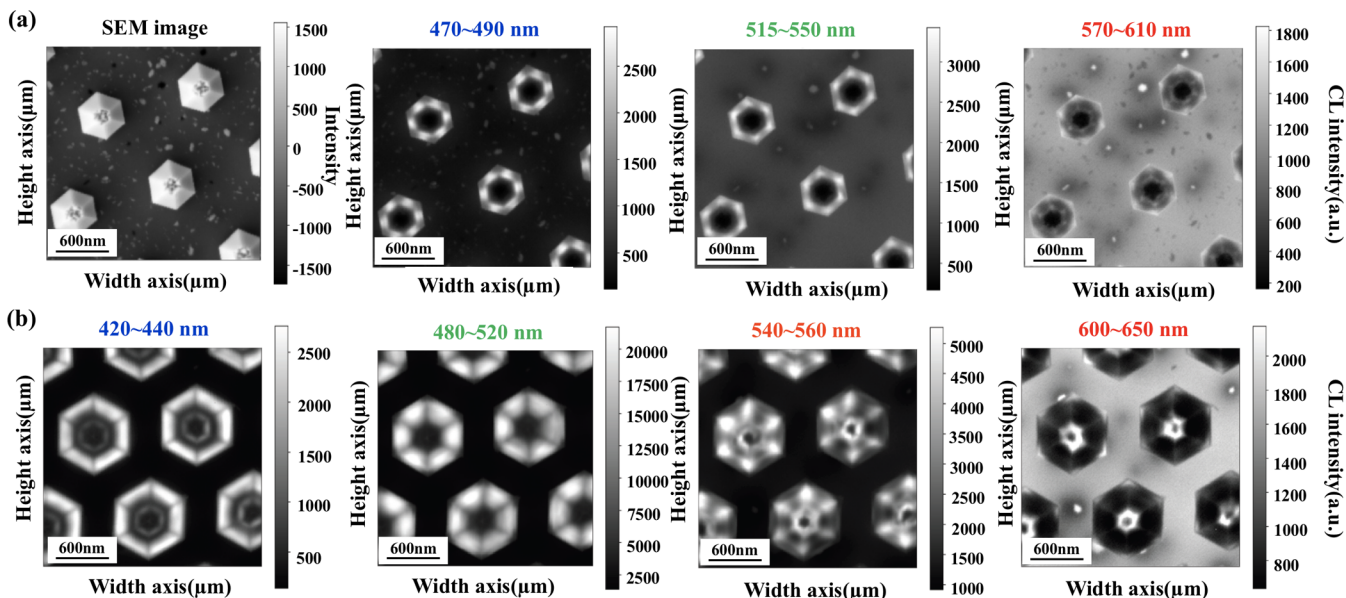


Figure 3. Planar-view SEM images and CL mappings measured at different emission wavelength ranges of NW arrays in sample a without SLs (a) and sample b with SLs (b).

$$E_f = E_{\text{ads}} - E_{\text{clean}} - (\Delta n_{\text{Ga}} \times \mu_{\text{Ga}} + \Delta n_{\text{In}} \times \mu_{\text{In}} + \Delta n_{\text{N}} \times \mu_{\text{N}}) \quad (2)$$

Here, E_{ads} and E_{clean} represent the total structure energy of epitaxial atoms after and before adsorption on the GaN surface, respectively. Δn denotes the number of atoms (Ga, In, or N) adsorbed on the GaN surface. In both formulas, the chemical potentials of the Ga, In, and N elements are marked as μ_{Ga} , μ_{In} , and μ_{N} . These chemical potentials follow the typical equilibrium conditions: $\mu_{\text{Ga}} + \mu_{\text{N}} = \mu_{\text{GaN}}$ and $\mu_{\text{In}} + \mu_{\text{N}} = \mu_{\text{InN}}$, where μ_{GaN} and μ_{InN} represent the chemical potentials of bulk GaN and InN, respectively. Notably, among the three elements (Ga, In, and N) in epitaxy, N is a common element in the epitaxy of both GaN and InN. Additionally, the formation energy of bulk GaN (ΔH_{GaN}) is 1.10 eV, which exceeds the formation energy of bulk InN (ΔH_{InN}) at 0.39 eV.^{36,37} Therefore, within the range of variations in the chemical potential of each element, μ_{N} was the sole variable, changing from $\mu_{1/2\text{N}_2} - \Delta H_{\text{GaN}}$ (representing Ga-rich growth conditions in GaN epitaxy) to $\mu_{1/2\text{N}_2}$ (representing N-rich conditions in GaN and InN epitaxy). Here, the $\mu_{1/2\text{N}_2}$ was inferred from N_2 molecules (-16.66 eV). Based on this, it was determined that the range of variations in the chemical formula of the N element during the reaction process was -8.33 eV (N-rich) to -8.72 eV (In-rich) and ultimately to -9.43 eV (Ga-rich).

3. RESULTS AND DISCUSSION

3.1. Morphology and Emission Properties of the GaInN/GaN NWs with SL Structures. The bird's-eye view SEM images and structure diagram of the NWs in sample a without SLs and sample b with SLs are shown in Figure 2a,b, respectively. Compared with sample a, the (1011)-plane in sample b tended to merge at the NW apex, resulting in the shrunk (0001) plane. To explore the effect of SLs on the morphology of NWs, detailed cross-sectional STEM characterization was carried out, as shown in Figure 2c,d. The thicknesses of both SL and MQS on the (0001) and (1010)-planes were greater than that on the (1011)-plane, which is attributable to the differential growth rates on the three crystalline planes. In addition, it was observed that the epitaxial layer of the (1011)-plane forms an "eave"-shaped structure near the junction between (1011) and (1010)-planes.

Specifically, the high-resolution STEM characterization in Figure 2d indicates the presence of ultrathin (1011)-plane SLs at the junction between the (0001)-plane SLs and the (1011)-plane MQS epitaxial layer. Because the periodic thickness of (1011)-plane SLs was extremely thin compared to that grown on other crystalline planes, it was difficult to exhibit effective trapping for point defects there. The effect of SLs in improving the quality of subsequent epitaxial MQS was evaluated by TRCL measurements, as plotted in Figure 2e. For sample a without SLs, the CL wavelengths of the MQS on the nonpolar, semipolar, and apex regions of the NWs were around 480, 515, and 600 nm, respectively. The corresponding carrier lifetimes, determined through single-exponential decay fitting of the TRCL curves, are 0.09, 0.11, and 0.17 ns. In contrast, for sample b, which contained SLs, the MQS region exhibited wavelengths of 500, 550, and 610 nm on the respective crystalline planes, with carrier lifetimes of 0.18, 0.28, and 0.20 ns. Additionally, the SLs in sample b show emission at wavelengths of 400 and 430 nm, with carrier lifetimes of 0.13 and 0.18 ns, respectively. The longer carrier lifetimes in sample b demonstrated that the quality of the active MQS region was significantly improved owing to the reduced nonradiative recombination centers by SLs. Figure 2f,g shows the TRCL mappings at the emission wavelength ranges of 405–490 and 465–550 nm for samples a and b, respectively. For sample a, the emission peak is mainly located around 470 nm and the corresponding carrier lifetime is mainly around 330 ps. In sample b with SLs, the signal of carrier lifetime located from 350 to 700 ps is clearly observed in the broad emission range of 465–550 nm owing to the suppression of point defects density by SLs. Compared with sample a, it is noteworthy that there is an increased lifetime distribution in the long-wavelength region in sample b. Thus, it is deduced that the alteration in the shape of the NWs due to the SLs may have influenced the InN fraction of the MQS. The incorporation of the SL structure led to an increase in NW diameter and a decrease in the spacing between NWs, promoting the incorporation of In atoms. Additionally, the SL structures contributed to strain relaxation within the MQSs. Collectively,

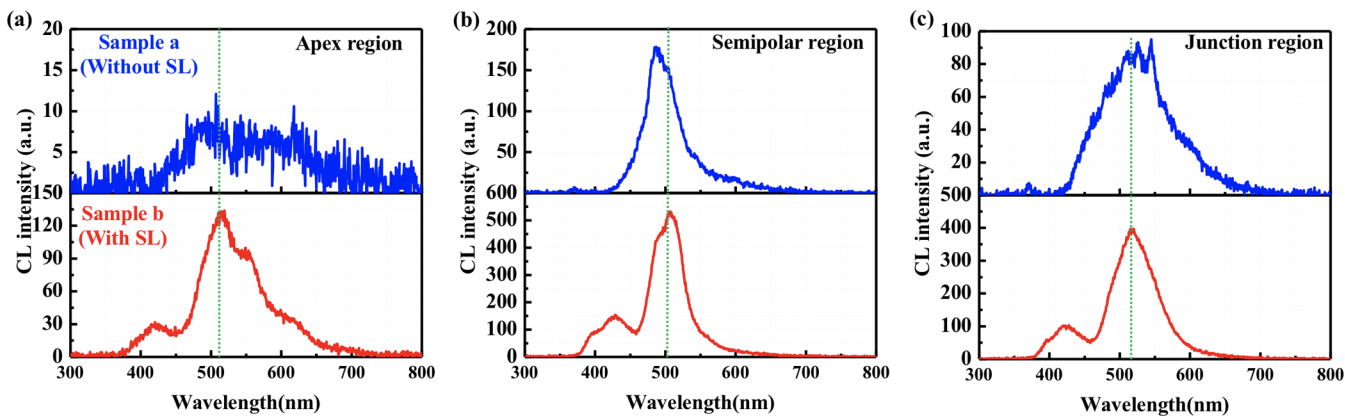


Figure 4. CL spectra of samples a and b at the (a) apex region, (b) center of the semipolar $(10\bar{1}1)$ -planes, and (c) junction region between the $(10\bar{1}1)$ -planes.

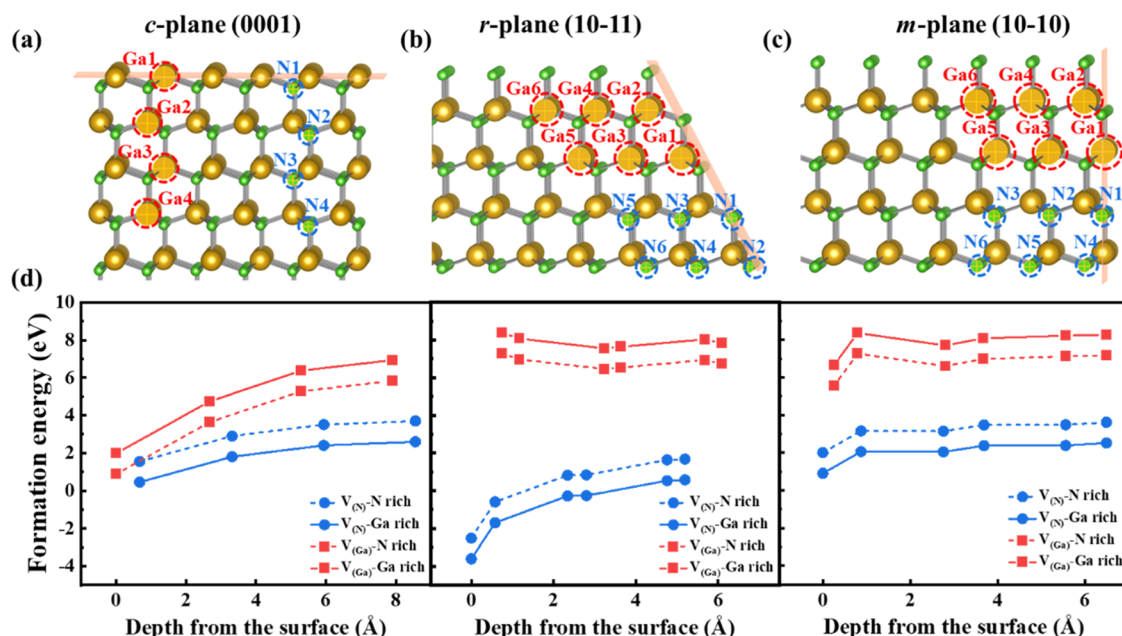


Figure 5. Schematic diagrams of vacancy models at different depths on the (a) (0001) -plane, (b) $(10\bar{1}1)$ -plane, and (c) $(10\bar{1}0)$ -plane regions of GaN NWs. (d) Formation energy of vacancies of the corresponding model diagram as a function of depth. The asterisks represent the formation energies of different types of cluster defects on the surface layer.

these factors resulted in a higher In composition in the active region of sample b, as confirmed by subsequent CL spectral measurements.

Figure 3a shows the planar-view SEM image and corresponding CL mappings of sample a. The SEM image reveals the uniform growth of NWs, despite the presence of a rough apex and the formation of In-rich crystalline particles on the SiO_2 mask. The emission at 470–490 and 515–550 nm was observed only at the periphery of the NWs. The short-wavelength emission region of 470–490 nm was distributed in the center area of the $(10\bar{1}1)$ -planes. Meanwhile, the green light emission band of 515–550 nm was positioned at the junction of $(10\bar{1}1)$ -planes, indicating that the corner area exhibits a higher In content. However, no obvious emission was detected at the apex of the NWs in any wavelength range. This is due to the roughness on the (0001) -plane and low quality of grown MQSs, as can be confirmed from the SEM image. Upon inserting an SL defect-blocking layer during the epitaxial process, the (0001) -plane of the NWs shrunk, while

the $(10\bar{1}1)$ -plane expanded, as depicted in Figure 3b. The emission in the wavelength region of 420–440 nm predominantly emanated from the periphery of the $(10\bar{1}1)$ -plane and apex region, primarily originating from the SL structures. The uniform emission in the wavelength region of 480–520 nm suggests a notable enhancement in the crystalline quality of MQS structures. Similar to the trends observed in sample a, the InN mole fraction also tended to be higher at the junction of the $(10\bar{1}1)$ -planes. This phenomenon is attributable to the release of strain energy through local deformation at these points in the NWs.^{38,39} The emission intensity at wavelength 600–650 nm of the NW apex region of sample b was increased in comparison to sample a, with a correspondingly larger area exhibiting bright emission. The introduction of SL structures increased the diameter of the NWs and improved the crystalline quality, resulting in promoted In incorporation and strong emission intensities. Most importantly, owing to the improved crystalline quality and (0001) -plane morphology of NWs, red-light emission was achieved in

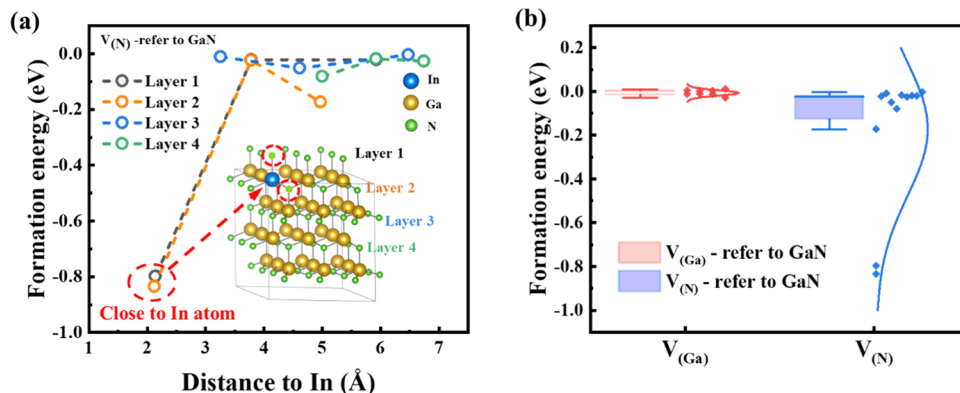


Figure 6. (a) Formation energies of $V_{(N)}$ at different positions within the GaInN SL layer with reference to zero energy, which is defined as the $V_{(N)}$ formation energy in GaN supercells. The inset depicts a model of the GaInN layer, highlighting the position of the $V_{(N)}$ proximity to the In atom. (b) The calculated $V_{(Ga)}$ and $V_{(N)}$ formation energies at different positions within the GaInN layer are compared with the distribution of vacancy formation energies in GaN supercells.

(0001)-plane MQSs, making sample b exhibit excellent emission characteristics in the longer wavelength range of 600–650 nm.

To confirm the specific emission wavelengths, the CL spectra were further acquired from the apex (0001)-plane region, semipolar (101̄1)-region, and junction region of the NWs in samples a and b, as depicted in Figure 4a–c, respectively. Compared with the spectra of sample a, the CL intensity of the NWs with SLs at three regions was found to be significantly stronger. In Figure 4a, unlike the faint emission observed in sample a, sample b demonstrates a prominent emission peak at a wavelength of 519 nm, as observed from the CL mappings. This enhancement indicates that the SLs have improved the crystalline quality of the (0001)-plane MQS structures. In addition, the emission peak at 420 nm peak was attributed to the presence of the SLs. The shoulder peaks at 550 and 600 nm originated from the MQS located on the tip of the NW, as revealed by CL mapping. By inserting SLs, the (0001)-plane MQS was reduced, enhancing its quality and enabling the observation of the strong emission peaks from the (0001)-plane MQS of the NWs. In Figure 4b, the CL peak wavelength of sample b exhibits a redshift of 19.5 nm accompanied by a 3-fold increase in emission intensity compared to that of sample a. The CL spectra measured at the junction region of (101̄1)-planes indicate that samples a and b emitted comparable peaks at approximately 520 nm, exhibiting a 4.2-fold enhancement. In both samples a and b, the peak wavelength at the junction area was longer than that at the (101̄1)-plane region, consistent with the observation in CL mappings.

3.2. Epitaxial Modeling of SL Structures on Different Planes of the GaInN/GaN NWs. As mentioned above, the SL structure is beneficial for suppressing the point defect density of subsequent epitaxial MQS structures. However, the epitaxial mechanisms and effect of SL on the point defects in GaInN/GaN NWs need to be further clarified. First, the vacancy formation energies on different crystalline surfaces were calculated to discuss the defect formation characteristics. Figure 5 shows the schematic diagram of vacancies at different depths on the surface of the GaN NW and the corresponding formation energies, where the depth represents the position of vacancy defects from the NW surface (orange plane in Figure 5a). Meanwhile, the formation energies of surface vacancy clusters were calculated, including the divacancies of $V_{(Ga)}$ –

$V_{(N)}$ and $(V_{(N)} - V_{(N)})$, as well as the trivacancies composed of double $V_{(Ga)}$ and a $V_{(N)}$ ($V_{(Ga)} - V_{(N)} - V_{(Ga)}$).^{40–42} The formation energies of $V_{(Ga)}$ near the surface decrease on the (0001) and (1010)-planes. However, this phenomenon was less pronounced on the (101̄1)-plane. From Figure 5d, one can see that the formation energies of $V_{(N)}$ are lower than that of $V_{(Ga)}$, indicating that $V_{(N)}$ is a dominant vacancy defect of each crystalline plane. The formation energies of $V_{(N)}$ are the lowest in the near-surface region, especially on the (101̄1)-plane. This indicates that $V_{(N)}$ easily forms in the outermost layer during the epitaxy process, implying a tendency for $V_{(N)}$ to mitigate from the interior of the GaN NW toward the epitaxial direction (i.e., the surface layer). This can increase the nonradiative recombination centers on the sidewall of GaN NWs. As the diffusion of $V_{(N)}$ progressed toward the subsequent epitaxial structures, the vacancy concentration in the GaInN quantum wells increases, impacting the device performance. Among the surface cluster defects, the formation energies of different types of vacancy clusters on the (0001) surface are relatively close. Notably, the formation energies of $V_{(Ga)} - V_{(N)}$ and $V_{(Ga)} - V_{(N)} - V_{(Ga)}$ clusters in (0001)-plane are significantly lower than that of other crystalline planes, indicating that $V_{(Ga)}/V_{(N)}$ complex cluster defects are dominant sources of nonradiative recombination centers on the (0001)-plane, which is consistent with the research results of Kojima et al.⁴³ Therefore, reducing the vacancy concentration in the n-GaN nanocores prior to the MQS growth is a key factor in improving the quality of NW-LED devices.

GaInN/GaN SLs are commonly applied prior active regions in semiconductor optoelectronic devices.^{26,44–46} However, the precise mechanism of this effect remains to be further understood, especially on different crystalline planes. Here, a $3 \times 3 \times 2$ GaN supercell and equivalent-sized GaInN alloy bulk model (with an In component equivalent to 2.78%) were constructed. The formation energies of $V_{(Ga)}$ and $V_{(N)}$ were calculated at various distances from the In atom and then compared with the point defect formation energy in the GaN supercell. Figure 6a illustrates the vacancy formation energies at different points in the GaInN SL layer, while the statistical distribution diagram is drawn in Figure 6b. Compared with GaN, the formation energies of $V_{(N)}$ near the In atom in the SLs are lower, with a maximum reduction of 0.84 eV. Additionally, the $V_{(N)}$ formation energies far from the In atom are also slightly reduced as compared with GaN. The

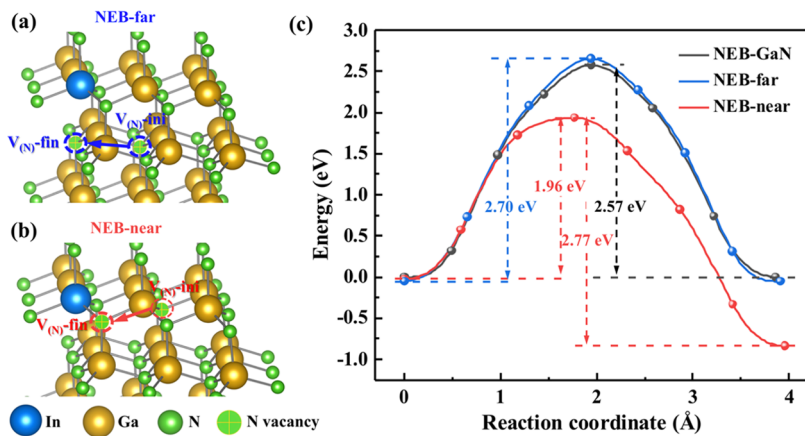


Figure 7. Schematic diagrams of $V_{(N)}$ migration paths in the GaInN layer far away from (a) and near (b) the In atom. (c) The migration barrier of $V_{(N)}$ in each reaction path, where the 0 energy is labeled as the $V_{(N)}$ formation energy in GaN supercells.

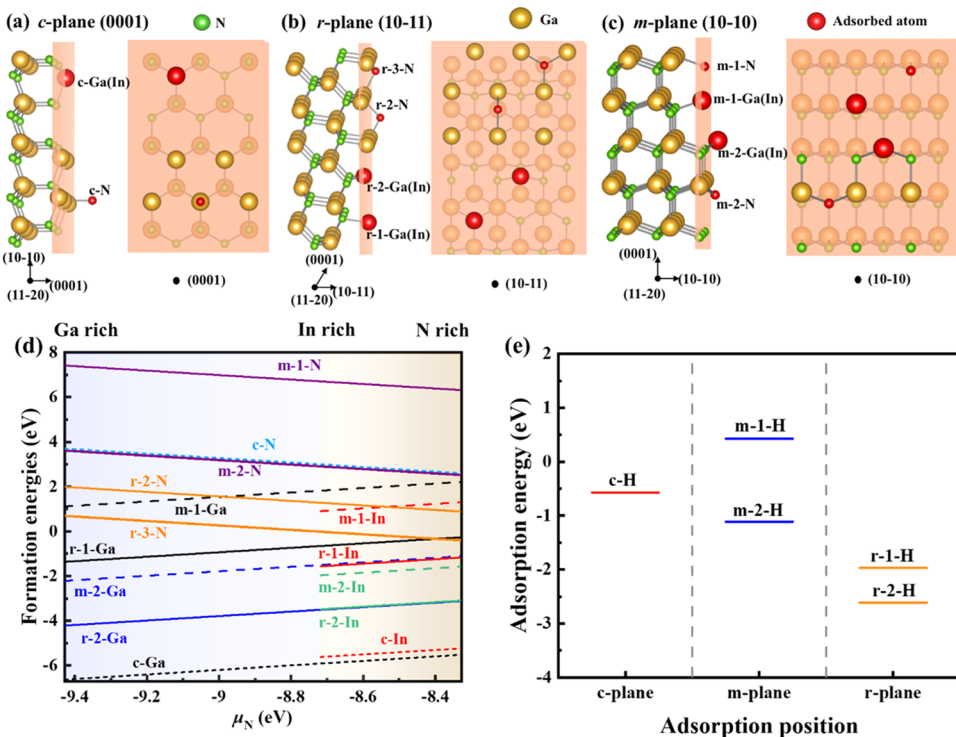


Figure 8. Schematic diagrams depict the model structure of atoms adsorbed on (0001)-plane (a), $(10\bar{1}1)$ -plane (b), and $(10\bar{1}0)$ -plane (c). (d) The relationship between the adsorption formation energy of adsorbed atoms at different crystal facets and their respective positions in relation to the chemical potential of N. (e) Adsorption energy of H atom on different crystalline planes of NWs.

formation energy characteristics of $V_{(\text{Ga})}$ in the GaInN SL layer were also analyzed. It is observed that the alterations in its formation energy are all below 0.1 eV when compared with GaN. This implies that the $V_{(\text{Ga})}$ within the SL layer closely resemble those in bulk GaN. Consequently, it could be inferred that owing to the favorable conditions for $V_{(N)}$ formation near the In atoms, the introduction of a thin GaInN layer in GaN is more likely to form $V_{(N)}$. These vacancies tend to cluster around the In atoms, ultimately reducing the migration of $V_{(N)}$ into subsequent epitaxial layers.

To delve deeper into the suppression effect of SLs on the migration of point defects in GaN epitaxial layers, the climbing image nudged elastic band (CI-NEB) method was employed to calculate the migration barriers of $V_{(N)}$ in the GaN and GaInN molecular layers. The migration path diagrams and

reaction barriers are depicted in Figure 7, wherein the calculations are denoted as NEB-GaN, NEB-far, and NEB-near, respectively. The reference point for the initial state formation energy of $V_{(N)}$ in GaN was set at 0. When $V_{(N)}$ is distant from the In atom within the low-In component of GaInN and migrates to the adjacent site (NEB-far), the migration needs to overcome a reaction barrier of 2.70 eV. The saddle point of this transition state is in the middle of the initial and final states, slightly above the $V_{(N)}$ migration barrier (2.57 eV) that was observed in GaN supercells, as denoted by NEB-GaN in Figure 7c. For $V_{(N)}$ near the In atom (NEB-near), the migration barrier from the site far away from the In atom to the In atom's edge is low, only 1.96 eV. Nevertheless, to migrate from the site near the In atom to the far end, the migration barrier is as high as 2.77 eV. This indicates that In

atoms can stabilize the $V_{(N)}$ surrounding it. Therefore, the GaInN layer exhibits the capability to attract $V_{(N)}$ during the vacancy migration process, blocking the point defects from migrating to the subsequent GaN epitaxial layers. This can result in an effective reduction in the point defect density within the subsequently grown MQS on GaN NWs. The findings here are consistent with the above experimental results, demonstrating that the increase in CL intensity is attributed to the improved quality of MQS resulting from the suppression of point defect propagation into MQS by SL structures.

To investigate the growth characteristics of the SLs on the different crystalline planes of the NWs, surface models of different crystalline planes of GaN were constructed. Subsequently, first-principles calculations were conducted to analyze the atomic adsorption characteristics. Since the atomic layer stacking configuration of high Miller index crystalline planes, like the (1011) and (10 $\bar{1}$ 0)-planes in the wurtzite GaN, differs from the AB stacking of the (0001)-plane, multiple adsorption sites became available for adsorbed atoms on these planes. To distinguish different atomic adsorption models, surface adsorption models were characterized based on the number of bonds formed when atoms were adsorbed onto the crystalline planes of the NWs, as illustrated in Figure 8a–c. Specifically, there were distinctive bonding interactions involving single-bond and double-bond interactions between the (1010)-plane surface and adsorbed atoms. These interactions are represented as m-1-X and m-2-X ('X' refers to Ga, In, or N atoms). The (10 $\bar{1}$ 1)-plane exhibited double- and triple-bond formations with adsorbed N atoms, while it demonstrated single-bond and double-bond interactions with the adsorbed group-III atoms. These interactions are denoted as r-2-N, r-3-N, r-1-X, and r-2-X, with 'X' representing Ga or In atoms. For the (0001)-plane, the adsorption model is simply denoted as c-X, where 'X' can refer to Ga, In, or N atoms.

Since the adsorption formation energies of adsorbed atoms can describe the adsorption strength of atoms, the adsorption formation energies of the atom at different surfaces on the NW were used to discuss the adsorption properties of the atom during the epitaxial process. The adsorption formation energies of each elemental atom on the NW surface are shown in Figure 8d. As the N chemical potential increased (N-rich condition), the adsorption formation energies of group-III atoms increase, while that of N atoms decrease. This feature is not conducive to the adsorption of group-III atoms. Disparities in the adsorption formation energies of the same elemental atom were also observed, and these differences were ascribed to the number of bonds at different binding sites on the same crystalline plane. Specifically, the differences in formation energies for In, Ga, and N atoms adsorbed on the (10 $\bar{1}$ 0)-plane at double-bond sites and single-bond sites are -2.88, -3.32, and -3.80 eV, respectively. The differences in formation energy between adsorbed atoms on the (10 $\bar{1}$ 1)-plane at multibonds sites and fewer bond sites are -1.92, -2.85, and -1.29 eV, respectively. Therefore, adsorbed atoms exhibit a pronounced preference for depositing at multibond sites, facilitating the formation of effective nuclei during surface deposition. Notably, when group-III atoms are adsorbed at single-bonding sites of (1010)-plane (m-1-X), it has the highest adsorption energy in the group-III atomic adsorption case. This indicates that such adsorption behavior constitutes an endothermic reaction and is not conducive to spontaneous formation. Thus, the (10 $\bar{1}$ 0)-plane surface with a single

dangling bond represents a stable surface state. For adsorbate atoms with the same number of bonds, the adsorption energies on the (1011)-plane are lower than that on the (1100)-plane, which facilitate the adsorption of atoms and accelerate the growth rate of the (1011)-plane. However, the higher adsorption energy of (1010)-plane leads to the migration of adatoms to the junction between the (10 $\bar{1}$ 0) and (1011)-planes, forming "eaves" there, as reported in our previous work.²⁷ Compared with N atoms, group-III atoms had extremely low adsorption energy on the (0001)-plane, leading to the significant interdiffusion between adatoms on the (0001) and (10 $\bar{1}$ 1)-planes. The interdiffusion of adsorbed atoms between different crystalline faces results in a different chemical potential environment for the adsorbed atoms. Considering the adsorption conditions on the (10 $\bar{1}$ 0) and (1011)-planes, the lower adsorption energy of In atoms at identical adsorption sites indicates that compared with Ga atoms, In atoms have a stronger adsorption affinity on the surface. The above calculations reveal that In atoms exhibit stronger adsorption stability on the (10 $\bar{1}$ 1)-plane in comparison to the (1100)-plane. Consequently, such a preference leads to a higher In content on the (10 $\bar{1}$ 1)-plane under certain growth conditions.

To gain further insight into SL growth on NWs, the role of H atoms in the epitaxial process was considered. It has been reported that N-terminated growth surface is generally saturated with H passivation which hinders the absorption of subsequent atoms due to the high affinity of H atoms with (1011)-planes GaN.^{47,48} To verify this mechanism and assess the impact of H passivation on the growth of NWs, the adsorption energy of H atom on different crystalline planes ($E_{H\text{-ads}}$) was calculated by the following formula

$$E_{H\text{-ads}} = E_{H\text{-surface}} - E_{\text{clean}} - \mu_H$$

where $E_{H\text{-surface}}$ and E_{clean} are the total energies of the GaN surface after and before the adsorption of H atoms, respectively. Considering the diversity of H sources during MOCVD epitaxy (hydrogen carrier gas, ammonia, organics, etc.) and the lower decomposition temperature of NH₃ molecules, the chemical potential μ_H of H atoms in NH₃ molecules was used for calculation, i.e.,

$$\mu_H = \frac{\mu_{\text{NH}_3} - \mu_{\frac{1}{2}\text{N}_2}}{3} = -3.74 \text{ eV}$$

The calculation mode employed the (0001)-plane with a stable Ga-face and the (1010)-plane with an N surface. In the former, surface atoms feature only a single dangling bond, while in the latter, surface atoms have both single- and double-bond sites. The adsorption structure diagram and adsorption energy of H atom on different planes are shown in Figure 8e. The calculated adsorption energy of H atoms on the (0001)-plane is -0.57 eV, while the values on the (10 $\bar{1}$ 1)-plane at the bonding adsorption points of r-1-H and r-2-H are -1.97 and -2.61 eV, respectively. For the (10 $\bar{1}$ 0)-plane, the adsorption energies of H atoms at distinct bonding points are 0.43 eV and -1.11 eV, denoted as m-1-H and m-2-H, respectively. Such variance in adsorption energy results in the (10 $\bar{1}$ 1)-plane exhibiting a higher affinity for adsorbing H atoms and forming high-strength bonds with them, thereby facilitating effective surface passivation. This indicates that although the adsorption formation energy of epitaxial atoms on the (10 $\bar{1}$ 1)-plane is lower than that on the (10 $\bar{1}$ 0)-plane, H atoms are more inclined to bond with N atoms on the (10 $\bar{1}$ 1)-plane, effectively occupying the adsorption sites of group-III atoms. Such a

process dominated the ultralow growth rate of the $(10\bar{1}1)$ -plane, which hindered the attainment of the required thickness for epitaxial SLs. This also explains the lower thickness of the SL structure of the $(10-11)$ -plane in Figure 2d compared to the (0001) -plane. To enhance the growth rate on the $(10\bar{1}1)$ -plane, it is necessary to adjust the H chemical potential and reduce gas fluxes, such as easily decomposable NH_3 , to mitigate the probability of H atom adsorption passivation on the $(10\bar{1}1)$ -plane. Such epitaxy modeling is consistent with the growth features of different crystalline planes in the NWs. Due to the passivation mechanism of hydrogen on the $(10\bar{1}1)$ -plane during the epitaxial process, the growth rate of the SL structure's epitaxial characteristics on the $(10\bar{1}1)$ -plane was significantly lower than that on other planes.

4. CONCLUSIONS

The fabrication and comparison of NWs without and with SLs were conducted to investigate the growth characteristics on different crystalline planes and the trapping effect of defects, as evidenced by STEM, TRCL, and CL characterizations. Analysis of STEM images revealed that the SLs grew on the $(10\bar{1}1)$ -plane exhibited a significantly lower growth rate compared to the (0001) and $(10\bar{1}0)$ -plane. Furthermore, the increased carrier lifetime confirmed that the GaInN/GaN SLs suppressed the propagation of point defects to the MQSs, thereby improving the growth quality. First-principles calculations demonstrated that the point defect of $\text{V}_{(\text{N})}$ is prone to form on the epitaxial surface of NWs, especially on the $(10\bar{1}1)$ -plane. The transition state analysis by the CI-NEB suggested that the insertion of GaInN/GaN SLs during the NWs epitaxy process could reduce the potential barrier for $\text{V}_{(\text{N})}$ to migrate toward In atoms. This confined $\text{V}_{(\text{N})}$ near In atoms, providing a mechanism for inhibiting the migration of point defects in SLs during epitaxy. Formation energy calculations were conducted for atomic adsorption on different crystalline planes of NWs, revealing the propensity for nucleation adsorption on each plane. This, combined with H passivation phenomena, explained the differences in growth rates among the different crystalline planes in the NWs, consistent with the experimental results. These findings offer valuable insights into the growth mechanisms of NWs and the improvement of emission efficiency in NW-based Micro-LEDs. According to the first-principles calculation results, an increase in the thickness of SLs and GaInN wells on the $(10\bar{1}1)$ -plane is necessary for further improvement of emission properties on the $(10\bar{1}1)$ -plane.

AUTHOR INFORMATION

Corresponding Authors

Weifang Lu — Fujian Key Laboratory of Semiconductor Materials and Applications, CI Center for OSED, Department of Physics, Xiamen University, Xiamen 361005, China; Future Display Institute in Xiamen, Xiamen 361005, China; orcid.org/0000-0001-6214-4024; Email: weilu.weif@xmu.edu.cn

Kai Huang — Fujian Key Laboratory of Semiconductor Materials and Applications, CI Center for OSED, Department of Physics, Xiamen University, Xiamen 361005, China; Future Display Institute in Xiamen, Xiamen 361005, China; Email: k_huang@xmu.edu.cn

Authors

Jinjian Yan — Fujian Key Laboratory of Semiconductor Materials and Applications, CI Center for OSED, Department of Physics, Xiamen University, Xiamen 361005, China

Soma Inaba — Department of Materials Science and Engineering, Meijo University, Nagoya 468-8502, Japan

Yang Bao — Fujian Key Laboratory of Semiconductor Materials and Applications, CI Center for OSED, Department of Physics, Xiamen University, Xiamen 361005, China

Yang Sun — Fujian Key Laboratory of Semiconductor Materials and Applications, CI Center for OSED, Department of Physics, Xiamen University, Xiamen 361005, China; orcid.org/0000-0002-4344-2920

Jinchai Li — Fujian Key Laboratory of Semiconductor Materials and Applications, CI Center for OSED, Department of Physics, Xiamen University, Xiamen 361005, China; Future Display Institute in Xiamen, Xiamen 361005, China

Motoaki Iwaya — Future Display Institute in Xiamen, Xiamen 361005, China

Junyong Kang — Fujian Key Laboratory of Semiconductor Materials and Applications, CI Center for OSED, Department of Physics, Xiamen University, Xiamen 361005, China; Future Display Institute in Xiamen, Xiamen 361005, China

Tetsuya Takeuchi — Department of Materials Science and Engineering, Meijo University, Nagoya 468-8502, Japan

Rong Zhang — Fujian Key Laboratory of Semiconductor Materials and Applications, CI Center for OSED, Department of Physics, Xiamen University, Xiamen 361005, China; Future Display Institute in Xiamen, Xiamen 361005, China

Satoshi Kamiyama — Department of Materials Science and Engineering, Meijo University, Nagoya 468-8502, Japan

Complete contact information is available at:

<https://pubs.acs.org/10.1021/acs.cgd.4c01388>

Author Contributions

¶J.Y. and S.I. contributed equally to this work. W.L. devised the experiments and calculations for this work. J.Y. did the simulations. W.L., S.I., and A.S. grew the NW samples using MOVPE. J.Y. and S.I. wrote the first draft of the manuscript. W.L., J.Y., and S.I. prepared all of the figures. W.L. analyzed the results and revised the manuscript. W.L. and J.Y. prepared the response to reviewers' comments and revisions. Y.B. joined the figure preparation and discussion. K.H., J.L., J.K., and R. Z. joined the discussion. S.K., K.H., and Y.S. joined the discussion and revised the manuscript. S.K., T.T., K.H., and M.I. contributed to the data analysis and supervised the project.

Notes

The authors declare no competing financial interest.

ACKNOWLEDGMENTS

The authors thank Dr. Marc Fouchier and Dr. Christian Monachon from Attolight for providing characterizations of CL mapping and TRCL. The authors with Xiamen University, China, acknowledge the National Key Research and Development Program of China (Grant Nos. 2023YFB3610300, 2022YFB3603604), National Natural Science Foundation of China (Grant No. 62404184), and Fundamental Research

Funds for the Central Universities (No. 20720230019). This work was partially supported by MEXT Private University Research Branding Project, JST A-STEP project (JPMJTR 201D), NEDO Advanced Research (22100378), and Grant-in-Aid for Scientific Research AA (22 H 0030400304).

■ REFERENCES

- (1) Ryu, J. E.; Park, S.; Park, Y.; Ryu, S. W.; Hwang, K.; Jang, H. W. Technological Breakthroughs in Chip Fabrication, Transfer, and Color Conversion for High-Performance Micro-LED Displays. *Adv. Mater.* **2023**, *35* (43), No. e2204947.
- (2) Parbrook, P. J.; Corbett, B.; Han, J.; Seong, T. Y.; Amano, H. Micro-Light Emitting Diode: From Chips to Applications. *Laser Photonics Rev.* **2021**, *15* (5), No. 2000133, DOI: 10.1002/lpor.202000133.
- (3) Ding, K.; Avrutin, V.; Izyumskaya, N.; Özgür, Ü.; Morkoç, H. Micro-LEDs, a Manufacturability Perspective. *Appl. Sci.* **2019**, *9* (6), No. 1206.
- (4) Wu, T.; Sher, C.-W.; Lin, Y.; Lee, C.-F.; Liang, S.; Lu, Y.; Chen, S.-W. H.; Guo, W.; Kuo, H.-C.; Chen, Z. Mini-LED and Micro-LED: Promising Candidates for the Next Generation Display Technology. *Appl. Sci.* **2018**, *8* (9), No. 1557.
- (5) Zhou, S.; Liu, X.; Yan, H.; Chen, Z.; Liu, Y.; Liu, S. Highly efficient GaN-based high-power flip-chip light-emitting diodes. *Opt. Express* **2019**, *27* (12), A669–A692.
- (6) Li, P.; Li, H.; Zhang, H.; Lynsky, C.; Iza, M.; Speck, J. S.; Nakamura, S.; DenBaars, S. P. Size-independent peak external quantum efficiency (>2%) of InGaN red micro-light-emitting diodes with an emission wavelength over 600 nm. *Appl. Phys. Lett.* **2021**, *119* (8), No. 081102, DOI: 10.1063/5.0061940.
- (7) Boussadi, Y.; Rochat, N.; Barnes, J.-P.; Bakir, B. B.; Ferrandis, P.; Masenelli, B.; Licita, C. Investigation of sidewall damage induced by reactive ion etching on AlGaN PESA for micro-LED application. *J. Lumin.* **2021**, *234*, No. 117937.
- (8) Fan, B.; Zhao, X.; Zhang, J.; Sun, Y.; Yang, H.; Guo, L. J.; Zhou, S. Monolithically Integrating III-Nitride Quantum Structure for Full-Spectrum White LED via Bandgap Engineering Heteroepitaxial Growth. *Laser Photonics Rev.* **2023**, *17* (3), No. 2200455, DOI: 10.1002/lpor.202200455.
- (9) Zhou, S.; Wan, Z.; Lei, Y.; Tang, B.; Tao, G.; Du, P.; Zhao, X. InGaN quantum well with gradually varying indium content for high-efficiency GaN-based green light-emitting diodes. *Opt. Lett.* **2022**, *47* (5), 1291–1294.
- (10) Zhuang, Z.; Iida, D.; Ohkawa, K. InGaN-based red light-emitting diodes: from traditional to micro-LEDs. *Jpn. J. Appl. Phys.* **2021**, *61*, No. SA0809, DOI: 10.35848/1347-4065/ac1a00.
- (11) Chen, Z.; Sheng, B.; Liu, F.; Liu, S.; Li, D.; Yuan, Z.; Wang, T.; Rong, X.; Huang, J.; Qiu, J.; et al. High-Efficiency InGaN Red Mini-LEDs on Sapphire Toward Full-Color Nitride Displays: Effect of Strain Modulation. *Adv. Funct. Mater.* **2023**, *33* (26), No. 2300042, DOI: 10.1002/adfm.202300042.
- (12) Takeuchi, T.; Sota, S.; Katsuragawa, M.; Komori, M.; Takeuchi, H.; Amano, H.; Akasaki, I. Quantum-confined stark effect due to piezoelectric fields in GaInN strained quantum wells. *Jpn. J. Appl. Phys.* **1997**, *36* (4A), L382–L385.
- (13) Kou, J.; Shen, C. C.; Shao, H.; Che, J.; Hou, X.; Chu, C.; Tian, K.; Zhang, Y.; Zhang, Z. H.; Kuo, H. C. Impact of the surface recombination on InGaN/GaN-based blue micro-light emitting diodes. *Opt. Express* **2019**, *27* (12), A643–A653.
- (14) Hahn, Y. B.; Choi, R. J.; Hong, J. H.; Park, H. J.; Choi, C. S.; Lee, H. J. High-density plasma-induced etch damage of InGaN/GaN multiple quantum well light-emitting diodes. *J. Appl. Phys.* **2002**, *92* (3), 1189–1194.
- (15) Zhu, Z.; Tao, T.; Liu, B.; Zhi, T.; Chen, Y.; Yu, J.; Jiang, D.; Xu, F.; Sang, Y.; Yan, Y.; et al. Improved Optical and Electrical Characteristics of GaN-Based Micro-LEDs by Optimized Sidewall Passivation. *Micromachines* **2023**, *14* (1), No. 10, DOI: 10.3390/mi14010010.
- (16) Yu, J.; Tao, T.; Liu, B.; Xu, F.; Zheng, Y.; Wang, X.; Sang, Y.; Yan, Y.; Xie, Z.; Liang, S.; et al. Investigations of Sidewall Passivation Technology on the Optical Performance for Smaller Size GaN-Based Micro-LEDs. *Crystals* **2021**, *11* (4), No. 403.
- (17) Wong, M. S.; Lee, C.; Myers, D. J.; Hwang, D.; Kearns, J. A.; Li, T.; Speck, J. S.; Nakamura, S.; DenBaars, S. P. Size-independent peak efficiency of III-nitride micro-light-emitting-diodes using chemical treatment and sidewall passivation. *Appl. Phys. Express* **2019**, *12* (9), No. 097004.
- (18) Chen, D.; Wang, Z.; Hu, F. C.; Shen, C.; Chi, N.; Liu, W.; Zhang, D. W.; Lu, H. L. Improved electro-optical and photoelectric performance of GaN-based micro-LEDs with an atomic layer deposited AlN passivation layer. *Opt. Express* **2021**, *29* (22), 36559–36566.
- (19) Tian, P.; McKendry, J. J. D.; Gong, Z.; Guilhabert, B.; Watson, I. M.; Gu, E.; Chen, Z.; Zhang, G.; Dawson, M. D. Size-dependent efficiency and efficiency droop of blue InGaN micro-light emitting diodes. *Appl. Phys. Lett.* **2012**, *101* (23), No. 231110, DOI: 10.1063/1.4769835.
- (20) Kamiyama, S.; Lu, W.; Takeuchi, T.; Iwaya, M.; Akasaki, I. Growth and Characterization of Core-Shell Structures Consisting of GaN Nanowire Core and GaInN/GaN Multi-Quantum Shell. *ECS J. Solid State Sci. Technol.* **2020**, *9* (1), No. 015007.
- (21) Katsuro, S.; Lu, W.; Ito, K.; Nakayama, N.; Inaba, S.; Shima, A.; Yamamura, S.; Jinno, Y.; Sone, N.; Huang, K.; et al. Dimension dependence of current injection path in GaInN/GaN multi-quantum-shell (MQS) nanowire-based light-emitting diode arrays. *Nanophotonics* **2023**, *12*, 3077–3087, DOI: 10.1515/nanoph-2023-0051.
- (22) Bi, Z.; Lu, T.; Colvin, J.; Sjogren, E.; Vainorius, N.; Gustafsson, A.; Johansson, J.; Timm, R.; Lenrick, F.; Wallenberg, R.; et al. Realization of Ultrahigh Quality InGaN Platelets to be Used as Relaxed Templates for Red Micro-LEDs. *ACS Appl. Mater. Interfaces* **2020**, *12* (15), 17845–17851.
- (23) Bi, Z. X.; Chen, Z.; Danesh, F.; Samuelson, L. From NanoLEDs to the Realization of RGB-emitting MicroLEDs. In *Semiconductors and Semimetals*; Jiang, H.; Lin, J., Eds.; Elsevier Academic Press Inc, 2021; Vol. 106, pp 223–251.
- (24) Bi, Z.; Lenrick, F.; Colvin, J.; Gustafsson, A.; Hultin, O.; Nowzari, A.; Lu, T.; Wallenberg, R.; Timm, R.; Mikkelsen, A.; et al. InGaN Platelets: Synthesis and Applications toward Green and Red Light-Emitting Diodes. *Nano Lett.* **2019**, *19* (5), 2832–2839.
- (25) Lu, W. F.; Goto, N.; Murakami, H.; Sone, N.; Iida, K.; Terazawa, M.; Han, D. P.; Iwaya, M.; Tekeuchi, T.; Kamiyama, S.; Akasaki, I. Controlled synthesis of nonpolar GaInN/GaN multiple-quantum-shells on GaN nanowires by metal-organic chemical vapour deposition. *Appl. Surf. Sci.* **2020**, *509*, No. 145271.
- (26) Inaba, S.; Lu, W. F.; Ito, K.; Katsuro, S.; Nakayama, N.; Shima, A.; Jinno, Y.; Yamamura, S.; Sone, N.; Huang, K.; et al. Superlattice-Induced Variations in Morphological and Emission Properties of GaInN/GaN Multiquantum Nanowire-Based Micro-LEDs. *ACS Appl. Mater. Interfaces* **2022**, *14*, 50343–50353.
- (27) Lu, W. F.; Sone, N.; Goto, N.; Iida, K.; Suzuki, A.; Han, D. P.; Iwaya, M.; Tekeuchi, T.; Kamiyama, S.; Akasaki, I. Effect of AlGaN undershell on the cathodoluminescence properties of coaxial GaInN/GaN multiple-quantum-shells nanowires. *Nanoscale* **2019**, *11* (40), 18746–18757.
- (28) Lu, W. F.; Miyamoto, Y.; Okuda, R.; Ito, K.; Sone, N.; Iwaya, M.; Tekeuchi, T.; Kamiyama, S.; Akasaki, I. Correlation between Optical and Structural Characteristics in Coaxial GaInN/GaN Multiple Quantum Shell Nanowires with AlGaN Spacers. *ACS Appl. Mater. Interfaces* **2020**, *12* (45), 51082–51091.
- (29) Kresse, G.; Furthmüller, J. Efficiency of ab-initio total energy calculations for metals and semiconductors using a plane-wave basis set. *Comput. Mater. Sci.* **1996**, *6* (1), 15–50.
- (30) Kresse, G.; Furthmüller, J. Efficient iterative schemes for ab initio total-energy calculations using a plane-wave basis set. *Phys. Rev. B* **1996**, *54* (16), No. 11169.
- (31) Perdew, J. P.; Burke, K.; Ernzerhof, M. Generalized gradient approximation made simple. *Phys. Rev. Lett.* **1996**, *77* (18), No. 3865.

- (32) Monkhorst, H. J.; Pack, J. D. Special points for Brillouin-zone integrations. *Phys. Rev. B* **1976**, *13* (12), No. 5188.
- (33) Perdew, J. P.; Chevary, J. A.; Vosko, S. H.; Jackson, K. A.; Pederson, M. R.; Singh, D. J.; Fiolhais, C. Atoms, molecules, solids, and surfaces: Applications of the generalized gradient approximation for exchange and correlation. *Phys. Rev. B* **1992**, *46* (11), No. 6671.
- (34) Miceli, G.; Pasquarello, A. Energetics of native point defects in GaN: A density-functional study. *Microelectron. Eng.* **2015**, *147*, 51–54.
- (35) Zhuang, Q. Q.; Lin, W.; Yang, W. H.; Yang, W. C.; Huang, C. C.; Li, J. C.; Chen, H. Y.; Li, S. P.; Kang, J. Y. Defect Suppression in AlN Epilayer Using Hierarchical Growth Units. *J. Phys. Chem. C* **2013**, *117* (27), 14158–14164.
- (36) Zoroddu, A.; Bernardini, F.; Ruggerone, P.; Fiorentini, V. First-principles prediction of structure, energetics, formation enthalpy, elastic constants, polarization, and piezoelectric constants of AlN, GaN, and InN: Comparison of local and gradient-corrected density-functional theory. *Phys. Rev. B* **2001**, *64* (4), No. 045208.
- (37) Zheng, T. C.; Lin, W.; Cai, D. J.; Yang, W. H.; Jiang, W.; Chen, H. Y.; Li, J. C.; Li, S. P.; Kang, J. Y. High Mg effective incorporation in Al-rich Al_xGa_{1-x}N by periodic repetition of ultimate V/III ratio conditions. *Nanoscale Res. Lett.* **2014**, *9*, No. 40.
- (38) Lu, P. F.; Sun, C.; Cao, H. W.; Ye, H.; Zhong, X. X.; Yu, Z. Y.; Han, L. H.; Wang, S. M. Strain induced composition profile in InGaN/GaN core–shell nanowires. *Solid State Commun.* **2014**, *178*, 1–6.
- (39) Griffiths, J. T.; Ren, C. X.; Coulon, P.-M.; Le Boulbar, E. D.; Bryce, C. G.; Girgel, I.; Howkins, A.; Boyd, I.; Martin, R. W.; Allsopp, D. W. E.; et al. Structural impact on the nanoscale optical properties of InGaN core-shell nanorods. *Appl. Phys. Lett.* **2017**, *110* (17), No. 172105, DOI: 10.1063/1.4982594.
- (40) Chichibu, S. F.; Shima, K.; Kojima, K.; Takashima, S.; Edo, M.; Ueno, K.; Ishibashi, S.; Uedono, A. Large electron capture-cross-section of the major nonradiative recombination centers in Mg-doped GaN epilayers grown on a GaN substrate. *Appl. Phys. Lett.* **2018**, *112* (21), No. 211901.
- (41) Shima, K.; Iguchi, H.; Narita, T.; Kataoka, K.; Kojima, K.; Uedono, A.; Chichibu, S. F. Room-temperature photoluminescence lifetime for the near-band-edge emission of (000 1̄) p-type GaN fabricated by sequential ion-implantation of Mg and H. *Appl. Phys. Lett.* **2018**, *113* (19), No. 191901.
- (42) Chichibu, S. F.; Hazu, K.; Ishikawa, Y.; Tashiro, M.; Namita, H.; Nagao, S.; Fujito, K.; Uedono, A. Time-resolved photoluminescence, positron annihilation, and Al_{0.23}Ga_{0.77}N/GaN heterostructure growth studies on low defect density polar and nonpolar freestanding GaN substrates grown by hydride vapor phase epitaxy. *J. Appl. Phys.* **2012**, *111* (10), No. 103518.
- (43) Kojima, K.; Horikiri, F.; Narita, Y.; Yoshida, T.; Fujikura, H.; Chichibu, S. F. Roles of carbon impurities and intrinsic nonradiative recombination centers on the carrier recombination processes of GaN crystals. *Appl. Phys. Express* **2020**, *13* (1), No. 012004.
- (44) Itakura, H.; Nomura, T.; Arita, N.; Okada, N.; Wetzel, C. M.; Chow, T. P.; Tadatomo, K. Effect of InGaN/GaN superlattice as underlayer on characteristics of AlGaN/GaN HEMT. *AIP Adv.* **2020**, *10* (2), No. 025133.
- (45) Yan, J. J.; Chen, X. L.; Kang, W. Y.; Li, S. P.; Kang, J. Y.; Lin, W. Orbital and electronic responses in the GaN/AlN quantum structures constructed on different crystal planes. *Appl. Phys. Express* **2022**, *15* (7), No. 071002.
- (46) Wang, Y. X.; Rong, X.; Ivanov, S.; Jmerik, V.; Chen, Z. Y.; Wang, H.; Wang, T.; Wang, P.; Jin, P.; Chen, Y. N.; et al. Deep Ultraviolet Light Source from Ultrathin GaN/AlN MQW Structures with Output Power Over 2 W. *Adv. Opt. Mater.* **2019**, *7* (10), No. 1801763.
- (47) Li, S. F.; Fuendling, S.; Wang, X.; Merzsch, S.; Al-Suleiman, M. A. M.; Wei, J. D.; Wehmann, H. H.; Waag, A.; Bergbauer, W.; Strassburg, M. Polarity and Its Influence on Growth Mechanism during MOVPE Growth of GaN Sub-micrometer Rods. *Cryst. Growth Des.* **2011**, *11* (5), 1573–1577.
- (48) Feenstra, R. M.; Dong, Y.; Lee, C. D.; Northrup, J. E. Recent developments in surface studies of GaN and AlN. *J. Vac. Sci. Technol., B: Microelectron. Process. Phenom.* **2005**, *23* (3), 1174–1180.



CAS BIOFINDER DISCOVERY PLATFORM™

CAS BIOFINDER HELPS YOU FIND YOUR NEXT BREAKTHROUGH FASTER

Navigate pathways, targets, and diseases with precision

Explore CAS BioFinder